Single mode Lamb wave excitation at high frequency-thickness products using a conventional linear array transducer

Konstantinos Tzaferis*, Morteza Tabatabaeipour, Gordon Dobie, David Lines, Charles N. MacLeod
Centre for Ultrasonic Engineering, Department of Electronic and Electrical Engineering, University of Strathclyde, Glasgow, G11XW, UK
* Corresponding author, e-mail: konstantinos.tzaferis@strath.ac.uk

Abstract
Lamb wave excitation at high frequency-thickness products offers a potential solution for high-resolution guided wave testing. The method is attractive for crack imaging and corrosion mapping, especially in hidden locations where direct access is limited. However, multiple modes may propagate, complicating signal interpretation, which is undesirable. In this work, a systematic approach is presented, in an effort to determine the influence of the key parameters related to single higher order Lamb wave mode excitation with a conventional linear array transducer. Specifically, a linear time delay law is used to enhance a targeted mode, while the array's length, pitch and apodisation profile remain to be optimally selected. First, an analytical solution is derived based on modal analysis. This provides a natural decomposition of the amplitude of a guided wave mode to the product of the response of a single element and the excitation spectrum, which is related to properties of the array. Then, a key observation is made, associating the excitation spectrum to the directivity function for bulk wave phased array steering. This allows the application of well established phased array analysis tools to guided wave phased array excitation. In light of this fact, minimisation of the spectrum's bandwidth, elimination of the grating lobes and derivation of an apodisation profile are performed, to enhance the purity of the targeted mode. Finally, experiments conducted on an aluminium plate verify the above theoretical results. The Full Matrix is acquired, and all signals are reconstructed synthetically.

Keywords: Lamb waves, Higher order mode region, Single mode excitation, Unidirectional propagation, Apodisation

1. Introduction

Ultrasonic guided waves (UGW) are extensively used in structural health monitoring and non-destructive evaluation applications. They are commonly employed for the inspection of a large variety of structural assets, such as pipelines, storage tanks and pressure vessels. In this work, attention is shifted to a special class of UGW, namely Lamb waves, propagating in plates or plate-like waveguides. Lamb waves decompose to symmetric or antisymmetric modes. They can be classified based on their frequency-thickness product [1,2], which determines their key properties, such as phase velocity, dispersion and modal density. The region below 10 MHz·mm has been extensively investigated by several authors, particularly for steel and aluminium samples [3–15]. Recently, there has been a research interest in the region above 15 MHz·mm [1,2,16–22], called here higher order mode region, which is very attractive, because of the potential for medium-range high-resolution inspection of relatively thick samples at high frequencies. For example, operation at 20 MHz·mm implies guided waves can be generated on a 10 mm thick plate with a 2 MHz probe. Potential applications include the in-service inspection of the annular plate of storage tanks [1], thickness gauging [20], crack imaging [23,24] and inspection for corrosion on pipe networks, especially in hidden locations, such as corrosion under piper supports [21,22].

Lamb waves are commonly excited with piezoelectric, laser or electromagnetic acoustic transducers [25]. Among others, piezoelectric transducer excitation includes wedge [18], comb [26], interdigital [13], periodic [27], phased comb [8,28] or apodised phased comb [29]. The latter is an extension of phased comb excitation, describing the case where both time delays and voltage amplitudes vary across the elements of a conventional 1-D linear array probe with individually addressable elements. Such arrays are commonly deployed for bulk phased array ultrasonic inspections due to their flexibility and therefore guided wave excitation utilising these probes is advantageous, as they are readily available and mature. However, transducer size constrains and scanning resolution requirements for common engineering structures obligate manufacturing usually above 1 MHz. Commonly, operation at low frequency thickness products is preferred [27,30,31], below 3.5 MHz·mm, as it is easier to target a single mode. However, this requires thin waveguides, approximately up to 3.5 mm thick. Recent work has shown potential in exciting Lamb waves around 10 MHz·mm [8,29,32]. Veit and Bélanger [8] reported the generation of a single Lamb wave mode using a 64-element phased array probe centred at 1.5 MHz on a 5 mm thick aluminium sample. They used a linear time delay law and uniform voltage amplitudes across the array elements. Cirtautas et al. [29] demonstrated the feasibility of generation of the symmetric mode $S3$ on a 10 mm sample with a linear 1 MHz array mounted on an angled wedge using a two-sided excitation approach. The interaction of $S3$ with corrosion-like defects was simulated, showing the potential of the mode for corrosion defect detection and classification.

Guided wave phased array excitation is influenced by two key objects, namely the excitation and frequency spectrum [7]. The frequency spectrum is determined by the temporal profile of the applied pressure load. This profile is defined as the convolution of the excitation signal and the impulse response of the array elements. In guided wave applications, the excitation signal is typically a finite-cycled toneburst, controlled by the centre frequency, number of cycles and applied window [15]. The impulse response of an element of the array depends on the specific array design and material properties. Although this response might vary across the elements of the array, these variations are usually small and thus all elements are considered identical. Ultimately, the frequency spectrum is a bandpass filter, characterised by its centre frequency and bandwidth [33]. To excite a single mode, a narrowband spectrum is preferred, as unwanted modes outside the band range are filtered out. The excitation spectrum depends on the number of elements, pitch, time delay law and apodisation profile employed. In the frequency-wavenumber domain, assuming linear time delays and uniform voltage amplitudes, the points (f, k) where the spectrum maximises appear as straight lines (excitation beams). Their slope is determined by the pitch and the applied linear time delay law. Among the infinitely many excitation beams, one passes through the origin of the frequency-wavenumber domain. In the frequency-phase velocity domain, this beam appears as a straight horizontal line at constant phase velocity. Commonly, the time delays are adjusted so that the same excitation beam crosses the desired wave mode at the centre frequency. This way the two spectra intersect on top of the targeted mode, which is then generated and propagates in the waveguide.

In this work, emphasis is placed on guided wave excitation at the higher order mode region, using a conventional linear array. Employing a linear time delay law, a single low dispersion higher order mode is targeted at 20 MHz·mm. For the first time, a systematic analysis for guided wave excitation is presented where the length, pitch and apodisation profile are appropriately determined to optimise single mode excitation. More specifically, the influence of the number of elements on the bandwidth of the excitation spectrum is investigated. The effect of the pitch on the elimination of the grating lobes is studied in detail. The possibility of enhancing the purity of the targeted mode using an apodisation profile is explored. Moreover, the targeted guided wave mode propagation is unidirectional. This is due to satisfaction of a condition involving the pitch and wavelength of the selected mode. All conditions presented in this work are derived analytically and verified experimentally.

The organization of this paper is as follows. First, in Section 2, a model based on modal analysis is derived. The array is modelled as a transient periodic pressure load acting on the top surface of the plate, leading to an explicit expression between the amplitudes of any mode and the parameters relevant to the excitation. Then, a set of conditions related to the number of elements, pitch and apodisation profile is provided in Section 3. In Section 4, experimental results are presented, using a dataset acquired with the Full Matrix Capture (FMC) method. Finally, in Section 5, key conclusions are drawn.

2. Analytical solution for the apodised phased comb array excitation problem based on modal analysis

Guided wave excitation studies are commonly based on a suitable analytical method. Among others, the normal mode expansion method [34,35] and methods based on integral transforms, such as the Fourier transform [7] are commonly utilised. This work presents an alternative technique based on modal analysis, to solve the apodised phased comb array excitation problem. Besides its natural simplicity, the method offers some advantages. Specifically, it treats transient loads directly, without having to express the input signal as a superposition of time harmonic excitation sources using a Fourier transform [34]. Furthermore, there is no need to define new concepts, such as a new orthogonality condition [34]. Throughout the analysis, all quantities remain finite.

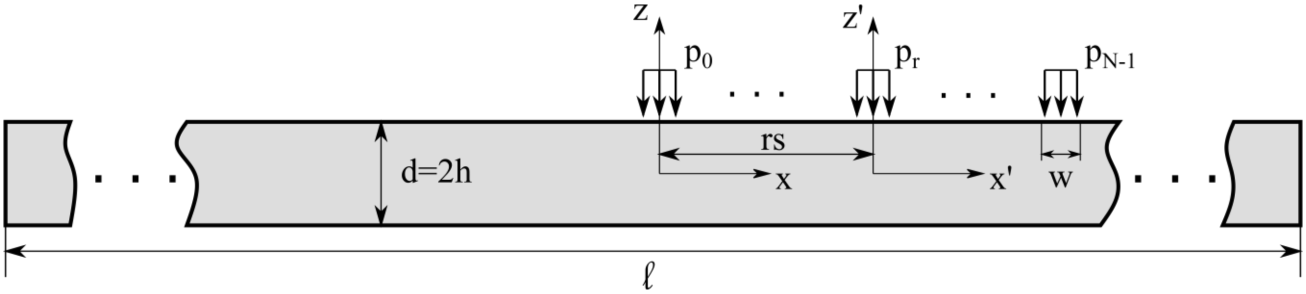

Figure 1. Apodised phased comb array excitation model. The plate has finite length $\boldsymbol{\ell}$ and thickness d. The pressure load $\boldsymbol{p_r}$ on the top surface of the plate models the rth element. A local frame $(\boldsymbol{x}', \boldsymbol{z}')$ is used to express the solution of the rth element. The global frame (x, z) coincides with the local frame of the first element.

Consider a homogeneous isotropic plate of length ℓ, thickness $d = 2h$ and width b. The equation of motion after omitting external loads appears in the form [7]

$$(\lambda + \mu)\nabla\left(\nabla \cdot \underline{u}\right) + \mu\nabla^2\underline{u} = \rho\underline{\ddot{u}}, \tag{1}$$

where λ, μ are the Lamé constants and ρ is the density of the plate. Assuming plane strain condition, the displacement field with respect to a right-handed frame (x, y, z) located at the centre of the plate appears in the form $\underline{u} = (u^1, 0, u^3)$. The cross section of the plate at $y = b/2$is shown in Figure 1. Separation of variables in space and time

$$u^1 = X^1(x)\, X^1(z)\, T(t), \qquad u^3 = X^3(x)\, X^3(z) T(t) \tag{2}$$

and after substituting (2) in (1) and employing the free-free boundary conditions on the top and bottom surfaces of the plate fully determines the through thickness profiles $X^1(z)$ and $X^3(z)$ of the modes in the axial and thickness direction, respectively [7]. Similarly, the modal profiles along the axial direction, $X^1(x)$ and $X^3(x)$, are determined by the boundary conditions on the left and right boundaries. However, in a guided wave excitation study, waves are assumed to propagate far from the left and right boundaries; thus, a particular choice of boundary conditions does not affect wave propagation. Therefore, the boundary conditions at the left and right edges can be arbitrarily chosen. In fact, any complete orthogonal set of functions in $L^2([-\ell/2, \ell/2])$ can be selected. In this work, the set $\left\{1, \cos(\mathrm{kx}), \sin(\mathrm{kx}) \mid k = \frac{2\pi\alpha}{\ell}, \alpha = 1,2,3\ldots\right\}$ is employed. As shown in [36], 'if $X^1(x)$ is a sine function, $X^3(x)$ must be a cosine function, and vice versa'. Note that for simplicity in notation, X is used to describe both the through thickness and axial displacement profiles, which are distinguished from the argument. The total solution can then be expanded in an infinite series form [37],

$$\underline{u} = \tau^i \underline{\hat{X}_i}, i = 1,2, \dots, \infty$$

where $\underline{\hat{X}_i}$ is the i^{th} normalised eigenfunction such that $\underline{\hat{X}_i} = \frac{1}{\sqrt{g_{ii}}}\underline{X_i}$ and g_{ij} is the metric tensor [38] defined as

$$g\left(\underline{X_i}, \underline{X_j}\right) = g_{ij} = b\int_{-h}^{h}\int_{-\ell/2}^{\ell/2} \rho \underline{X_i}\,\underline{X_j}\, dx\, dz.$$

The time dependent coefficients τ^i are determined according to [37]

$$\ddot{\tau}^i + \omega_i^2 \tau^i = f_i,\ f_i = \int_{-l/2}^{l/2} p(x,t)\, \hat{X}_i^3(x)\, \hat{X}_i^3(z = h)\, dx, \tag{3}$$

where the eigenfrequency ω_i related to mode $\underline{\hat{X}_i}$ is determined from the dispersion equations and

$$p(x,t) = \sum_{r=0}^{N-1} p_r$$

is the excitation load modelling an array with N elements, width w and pitch s, as shown in Figure 1. The size of the elements in the y-direction is assumed to be much larger than their width (x-direction); therefore, the plane strain condition holds [7]. In what follows, emphasis is placed on deriving an analytical expression for the u^3 component of the displacement field at the top surface of the plate. This is meaningful, as this is exactly the component sampled by a linear array. For simplicity in the notation, $u^3(x,h,t)$ is denoted as $u(x,t)$. The expression for u^1 and other fields, such as velocity or stress fields, is similar.

The solution for an arbitrary element r of the array is expressed in the local frame $x' = x - rs, t' = t - t_r$, as shown again in Figure 1. The excitation load is given by

$$p_r(x',t') = A_r g(x';w)h(t';M), \tag{4}$$

where A_r and $t_r = r\tau$ are the maximum voltage amplitude and linear time delay applied to the r^{th} element, respectively, $h(t')$ is an M-cycle normalised toneburst with centre frequency f_e and $g(x';w)$ is the normalised pressure distribution which is considered identical for all elements and is usually modelled as piston-source, parabolic-source distribution or a similar window function of width w. Substitution of (4) into (3) assuming zero initial conditions and neglecting the initial time $t' < M/f_e$, yields the solution of the time coefficients of the r^{th} sub-problem according to Duhamel's integral,

$$\tau_r^i(t') = \int_0^{M/f_e} \int_{-l/2}^{l/2} p_r(x,\tau)\, \hat{X}_i^3(x) \hat{X}_i^3(z=h)\ \sin\big(\omega_i(t'-\tau)\big)\, dx\, d\tau\ . \tag{5}$$

Equation (5) can be expressed as a sum of harmonic waves,

$$\tau_r^i(t') = A\cos(\omega_i t') + B\sin(\omega_i t')$$

and after straightforward manipulations and omitting index i for simplicity in the notation, the displacement field can be expressed in the form of forward and backward travelling waves,

$$u_r = A_s A_r e^{j(kx' \mp \omega t' - \psi)},$$

where only the real part of the expression is kept. The term A_s appears in the form

$$A_s(\omega,\mathrm{k}) = \frac{1}{2\omega}\hat{X}^3(h)^2 \sqrt{\left(\int_0^{M/f_e} h(t)\cos(\omega t)\,dt\right)^2 + \left(\int_0^{M/f_e} h(t)\sin(\omega t)\,dt\right)^2}\ \left|\int_{-w/2}^{w/2} g(x)\cos(kx)\,dx\right|.$$

Term A_s fully describes the modal amplitude distribution from the response of a single element. It can be decomposed in three terms; the first is known as the excitability function, defined as

$$E = \frac{1}{2\omega}\frac{X^3(h)^2}{g(X,X)}.$$

This term is related to the properties of the waveguide and cannot be altered. The normalised excitability function for the first 10 guided wave modes on a 10 mm thick aluminum plate is shown in Figure 2a. The modes exhibit a transient behavior until they reach a local maximum, after which the amplitude is strictly decaying. At high frequencies, modes $A0$ and $S0$ combine and form the Rayleigh wave [18], whose excitability remains constant with frequency. Figure 2b displays the excitability of the same modes at 2 MHz. Neglecting the Rayleigh wave, the excitability is strictly increasing from mode $A1$ to $A5$. The second term is the frequency spectrum, which can be interpreted as the norm of the Fourier transform of $\mathrm{h(t)}$,

$$\|\mathcal{F}(\mathrm{h(t)})\| = \left\|\int_{-\infty}^{\infty} \mathrm{h(t)}e^{-i\omega t}\mathrm{dt}\right\| = \sqrt{\left(\int_0^{M/f_e} h(t)\cos(\omega t)\,dt\right)^2 + \left(\int_0^{M/f_e} h(t)\sin(\omega t)\,dt\right)^2}\ .$$

The temporal profile of the applied load $h(t)$ can be seen as the convolution of the excitation signal and the impulse response of an array element. The third term is called single element excitation spectrum, given by

$$\mathrm{H_{se}} = \left|\int_{-w/2}^{w/2} g(x)\cos(kx)\,dx\right|.$$

This term depends on the element width and spatial pressure distribution profile. Assuming piston-like excitation, the single element spectrum for element width 1 mm is shown in Figure 3a. The maximum value is reached at $k = 0$ rad/mm, while several local minima and maxima occur in the displayed range. However, Lamb wave modes around 20 MHz·mm propagate at wavenumbers below 4 rad/mm. The effect of element width in this range is shown in Figure 3b. The amplitude of high-wavenumber modes is reduced with increasing element width. For example, at $k = 3.5$ rad/mm, the amplitude drop is -1.1, -5 and -14.5 dB for element width 0.5, 1 and 1.5 mm, respectively. Therefore, it is expected that more energy is distributed to lower wavenumber modes when increasing element width.

Linearity of (3) permits the expression of the total displacement field as a superposition of the individual solutions of each element. These solutions are then transformed to the global frame and summed according to

$$u = \sum_{r=0}^{N-1} u_r = \sum_{r=0}^{N-1} A_s A_r e^{j(kx' \mp \omega t' - \psi)} = A_s \sum_{r=0}^{N-1} A_r e^{j(kx - krs \mp \omega t \pm \omega r\tau - \psi)} = N A_s H_\pm e^{j(kx \mp \omega t - \psi - \phi)}$$

where

$$H_\pm(\omega, k) = \frac{1}{N}\sqrt{\sum_{r=0}^{N-1} A_r^2 + 2\sum_{r=0}^{N-1}\sum_{q=0}^{r-1} A_r A_q \cos\big((ks \mp \omega\tau)(r - q)\big)} \tag{6}$$

and ψ, ϕ are phase values and do not affect modal amplitudes. The above form of the spectrum holds for linear time delay law and arbitrary apodisation profile. It is important to note that the modal amplitudes can be decomposed to

$$A_\pm = A_S H_\pm, \tag{7}$$

where $A_S = NA_s$. Term A_s is related solely to the response of a single element; thus, it is determined by the frequency spectrum, mode excitability and element width. Multiplication by N is merely rescaling and thus insignificant. On the other hand, the excitation spectrum is strictly related to properties of the array, namely the pitch, number of elements, time delay law and apodisation profile. In the following section, the properties of the excitation spectrum are investigated in detail, to derive a set of conditions for single mode excitation.

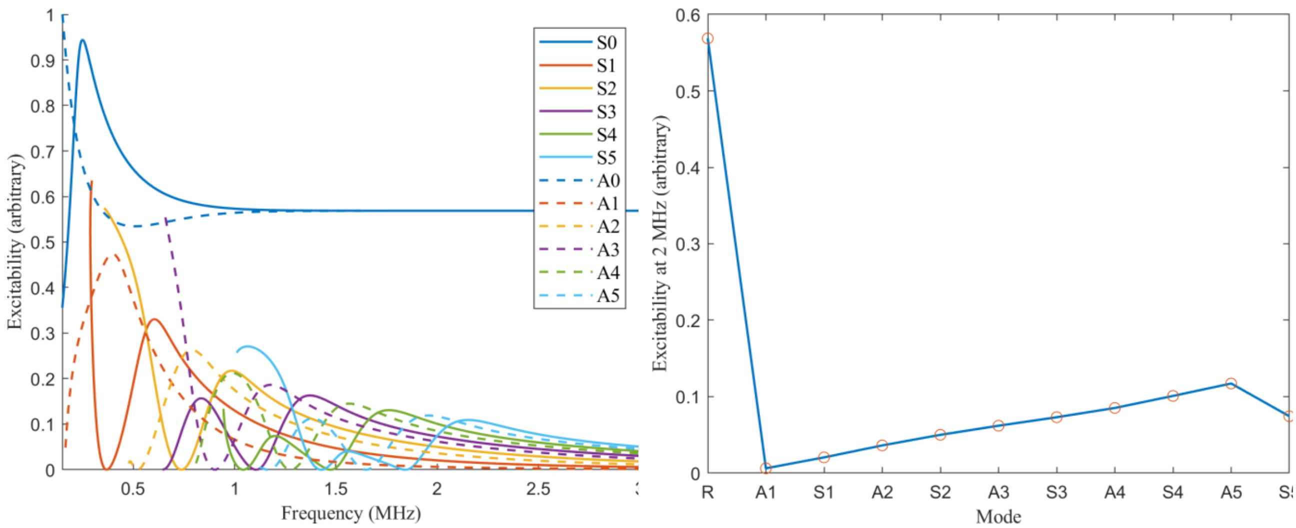

Figure 2. Excitability function for a 10 mm thick aluminium 6082-T6 plate. a) Excitability function of the first 10 modes. b) Excitability function of the same modes at 2 MHz.

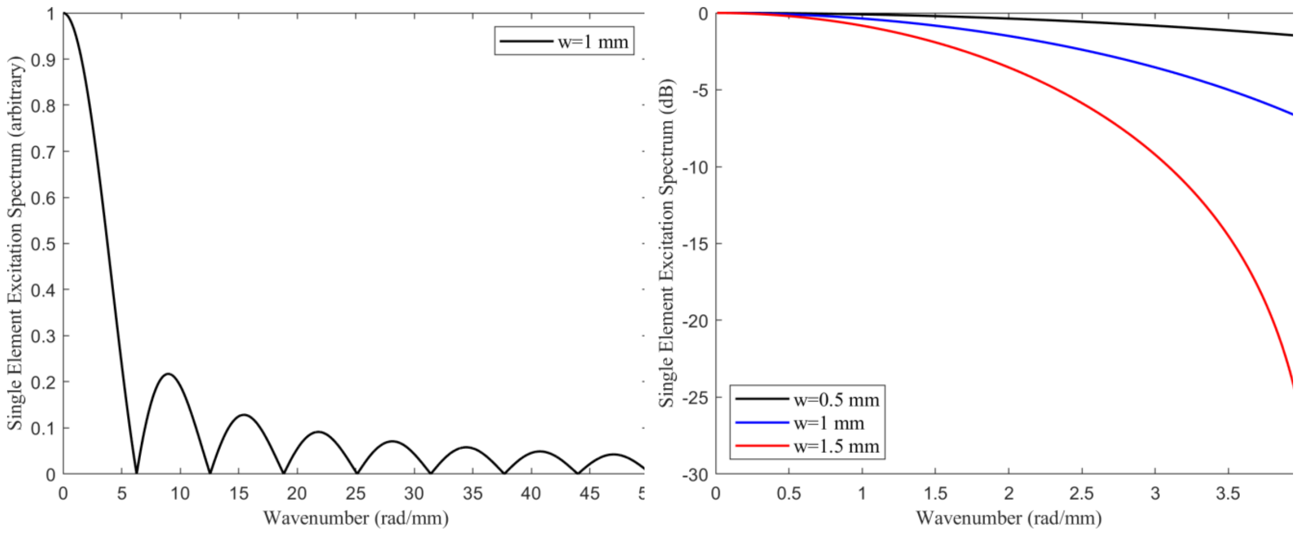

Figure 3. Single element excitation spectrum. a) Excitation spectrum for element width 1 mm. b) Excitation spectrum for element width w=0.5,1 and 1.5 mm. Higher wavenumbers are attenuated with increasing element width.

3. Selection of excitation parameters to enhance the purity of a single mode

If uniform amplitudes $A_r = 1$ are considered, the excitation spectrum (6) simplifies to

$$H_{\pm}(\omega, k\,;\,N, s, \tau) = \left|\frac{\sin\left(\frac{1}{2}N(ks \mp \omega\tau)\right)}{N\sin\left(\frac{1}{2}(ks \mp \omega\tau)\right)}\right|. \tag{8}$$

The spectrum depends on angular frequency and wavenumber, while the number of elements, pitch and time delay law are treated as parameters. Furthermore, using the transformations $\omega = 2\pi f, c_p = \frac{\omega}{k}$ *and* $k = \frac{2\pi}{\lambda}$, equivalent representations such as $H_{\pm}(f, c_p; N, s, \tau)$ can be obtained. To enhance the forward propagation of a mode, say at (f_e, c_{pe}), the time delay constant is selected to maximise $H_{+}(\omega_e, k_e)$, requiring the denominator of the same expression to vanish [28],

$$\sin\left(\frac{1}{2}(k_e\, s - \omega_e\, \tau)\right) = 0 \;\Rightarrow \tau = \frac{s}{c_{pe}} - \frac{n}{f_e}, \tag{9}$$

where $n \leq s\frac{c_{pe}}{f_e}$ and is an integer. For $n = 0$, the method is known as excitation at constant phase velocity [8].

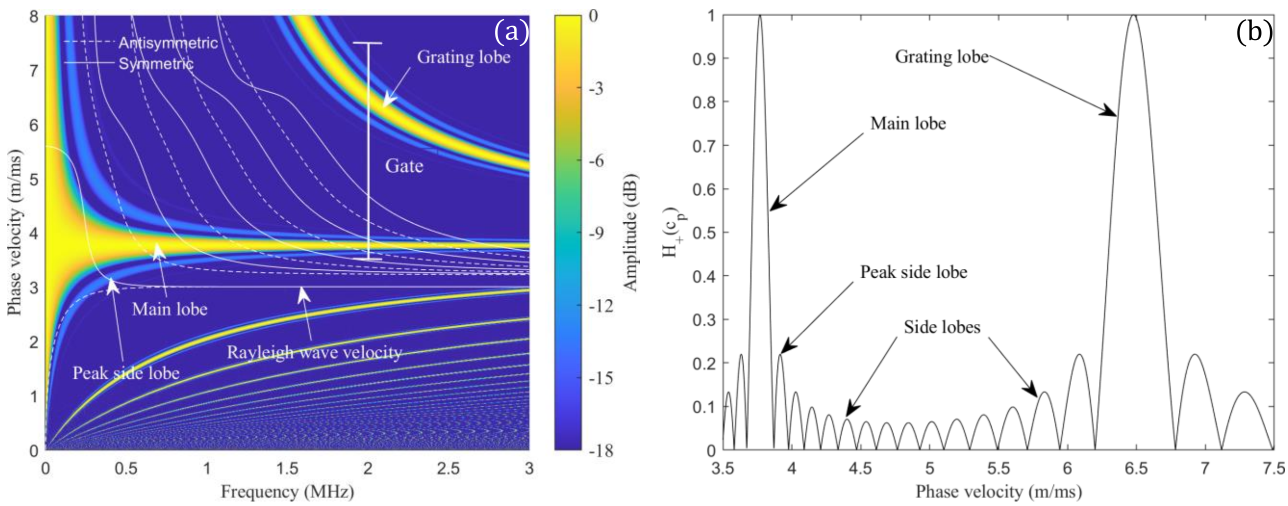

Figure 4. Excitation spectrum $\boldsymbol{H_+}$ for a 16-element array with pitch 4.5 mm. a) Spectrum at frequency-phase velocity domain. The main lobe is at constant phase velocity. One grating lobe above the Rayleigh wave velocity

is shown. The white lines represent dispersion curves of a **10** mm thick aluminium sample. b) Gated signal at 2 MHz, showing the main, grating and side lobes.

The excitation spectrum $H_+(f, c_p\ ;\ N, s, \tau)$ for a 16-element array with pitch 4.5 mm on top of the dispersion curves (in white) of a 10 mm thick aluminium plate is shown in Figure 4a. Although the pitch value is not representative of a conventional linear array probe, it is selected here to make it simpler to illustrate the attributes of the spectrum, namely the main, grating and side lobes. The time delay constant is set to $\tau = s/c_{pe} = 1194$ ns to enhance $S3$ with $(f_e, c_{pe}) = (2\ \text{MHz}, 3.77\ \text{m/ms})$. The excitation beam at constant phase velocity is shown (main lobe), while several excitation beams appear below and above c_{pe} (grating lobes). Fortunately, not all these beams are relevant to guided wave excitation. This is based on the fact that all guided wave modes lie between a well-defined region bounded by the Rayleigh wave V_R and cutoff velocity V_{cutoff},

$$V_R \leq c_p \leq V_{\text{cutoff}},$$

thereafter referred to as the excitable phase velocity region. Therefore, beams outside this region do not intersect with a guided wave mode and thus have no effect on guided wave excitation. For common steel and aluminium samples, $V_R \approx 3$ m/ms and $V_{\text{cutoff}} \approx 22$ m/ms. The excitation spectrum captured by the gate at $f = f_e$ is shown in Figure 4b. The spectrum consists of the main, side and grating lobes. Note that the display dynamic range in Figure 4a thresholds all but the biggest amplitude side lobes.

The features of the excitation spectrum in Figure 4b are familiar from bulk wave steering. In fact, direct comparison of (8) with the directivity function [39] for phased array steering $H_2(\theta)$ reveals that setting

$$sin\theta = \pm\frac{c_p\tau}{s} \text{ and } \sin\theta_s = 1, \tag{10}$$

it turns out that

$$H_2(\theta) = H_{\pm}, \tag{11}$$

where θ, θ_s are the azimuthal and steering angles with respect to the centre of the array, respectively. This means the material for phased array beam steering is transferable to phased array guided wave excitation. However, the performance of the array is not tested against angle θ but phase velocity, which is not a material constant due to the multimodal and dispersive nature of guided waves. Note also that setting $sin\theta_s = \pm\frac{c_p\tau}{s}$ and $\sin\theta = 1$ yields identical results, however, the former choice is made.

In what follows, emphasis is placed on the main attributes of the spectrum to improve guided wave excitation. More specifically, in Section 3.1, the bandwidth of the excitation spectrum is defined and an explicit form relating its width to relevant excitation parameters is provided. In Section. 3.2, a set of conditions on the pitch of the array are derived, to eliminate the grating lobes in the excitable phase velocity region. Finally, the general form of the spectrum is re-considered and an optimised apodisation profile is derived to further enhance the purity of the targeted mode in Section 3.3.

3.1 Bandwidth of excitation spectrum at constant phase velocity

At high frequency-thickness products, the low dispersion modes can be roughly approximated as straight horizontal lines in the frequency-phase velocity domain. Each mode can be associated with a phase velocity bandwidth, defined as

$$\Delta c_p^{m\pm} \equiv \left|c_p^m - c_p^{m\pm1}\right|,$$

where c_p^m the phase velocity of mode m and c_p^{m-1}, c_p^{m+1} the phase velocity of the modes closest to m such that $c_p^{m-1} < c_p < c_p^{m+1}$. The above definition is useful, as it quantifies how ‘far’ the examined mode is from its neighbours. The phase velocity bandwidth of $S3$ at 20 MHz·mm is shown in Figure 5.

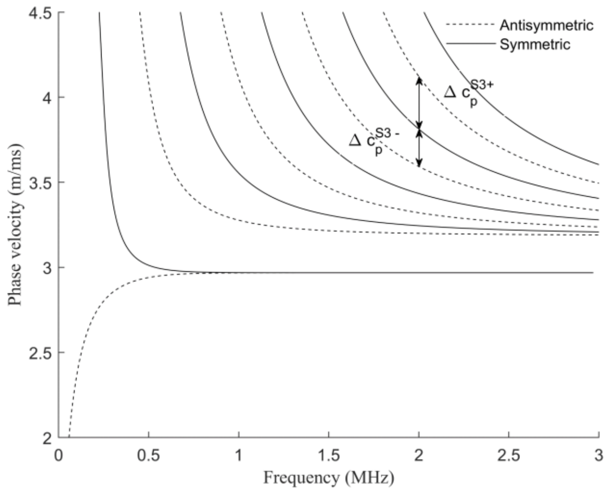

Figure 5. Phase velocity bandwidth of mode $\boldsymbol{S3}$ at 2 MHz on a 10 mm aluminium plate.

Next, the attention is shifted to the phase velocity bandwidth Δc_p of the excitation beam at constant phase velocity c_{pe} of the spectrum H_+. Based on the above, single mode excitation requires

$$\Delta c_p/2 < \Delta c_p^{m+} \ and \ \Delta c_p/2 < \Delta c_p^{m-} \tag{12}$$

where Δc_p is defined as the phase velocity interval containing the main lobe together with the left and right peak side lobes, see Figure 6. More specifically, using (46) from [39] and (10) the phase velocity corresponding to the local maxima of the first three side lobes, located on the right-hand side of the main lobe reads

$$c_p \approx \left(1 - \frac{(2m''+1)\lambda_e}{2Ns}\right) c_{pe}, \quad m'' = -2, -3, -4 \tag{13}$$

with corresponding amplitudes at -13.5 dB, -18 dB and -21 dB, respectively, as shown again in Figure 6. Including the peak side lobes in the definition of the bandwidth ensures the maximum amplitude outside the bandwidth region is not greater than -18 dB. Note that in the above equation, the dispersion effects are neglected. This is a valid assumption for the low dispersion modal region. For example, when $S3$ is targeted, the error between the exact phase velocity value corresponding to the maximum of the peak side lobe and (13) is less than 0.1%. Employing (29) from [39] and (10) and setting $m = \pm 2$, Δc_p is given by

$$\Delta c_p \approx \left(\left(1 + \frac{2\lambda_e}{Ns}\right) - \left(1 - \frac{2\lambda_e}{Ns}\right)\right) c_{pe} = \frac{4\lambda_e}{Ns} c_{pe}.$$

The above equation shows that the bandwidth of the excitation spectrum increases for increasing the wavelength and phase velocity of the targeted mode, but decreases when the total length of the array increases. This can be achieved by increasing the number of elements or the pitch. However, as will be shown in Section 3.2, increasing the pitch can have negative effects, as grating lobes may appear. The phase velocity bandwidth of $S3$ at 20 MHz·mm and the bandwidth of the excitation spectrum corresponding to an array with pitch 0.75 mm operating at 2 MHz for $32, 64$ and 128 elements are given in Table 1. We observe that $\Delta c_p^{m-} < \Delta c_p^{m+}$, which suggests that the modal density increases for lower phase velocities. The minimum number of elements to satisfy condition (12) using the same array is given by

$$\Delta c_p/2 < \Delta c_p^{S3-} \Rightarrow N > \frac{2\lambda_e}{\Delta c_p^{S3-} s} c_{pe} \Rightarrow N > 90,$$

which suggests $S3$ can be excited efficiently with an array length above 68 mm.

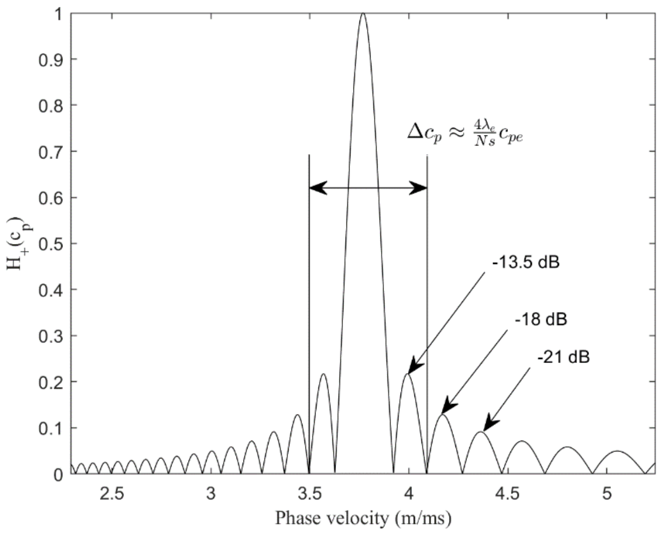

Figure 6. Excitation spectrum $\boldsymbol{H_+}$ at 2 MHz for a 64-element, 0.75 mm pitch array. The maximum amplitude of the peak, second and third side lobes is shown. The phase velocity bandwidth is defined as the width of the main and peak side lobes.

Table 1 Phase velocity bandwidth at **2** MHz of mode $\boldsymbol{S3}$ and a 0.75 mm pitch array with 32, 64 and 128 elements.

Mode/Spectrum	Phase velocity (m/ms)	Δc_p^{S3+} (m/ms)	Δc_p^{S3-} (m/ms)	$\Delta c_p/2$ (m/ms)
S3	3.77	0.32	0.21	-
32 −element array	3.77	-	-	0.59
64 −element array	3.77	-	-	0.30
128 −element array	3.77	-	-	0.15

3.2 Elimination of grating lobes in the excitable phase velocity region

The grating lobes correspond to local maxima of the excitation spectrum and are found by setting the denominator of the spectrum H_+ to zero. Combining (33) of [39] and (10), their location is determined according to

$$c_p(m') = \left(1 - \frac{m'\lambda}{s}\right)\frac{s}{\tau}, \tag{14}$$

where m' is an integer and $\lambda = c_p/f$. For the general linear time delay law given in (9) the main lobe occurs for $m' = n$, while $m' \neq n$ corresponds to grating lobes. Therefore, there exists an infinite number of grating lobes. Nevertheless, as stated earlier, only lobes that lie in the excitable phase velocity region are relevant. To eliminate them in this region, two necessary conditions are required. The first requires the lobe at the right $m' = n - 1$ (see Figure 4b) of the main lobe to occur at phase velocity higher than the cutoff,

$$c_p(m' = n - 1) > V_{cutoff}. \tag{15}$$

The second condition requires the lobe at the left $m' = n + 1$ of the main lobe to occur at phase velocity lower than the Rayleigh wave velocity,

$$c_p(m' = n + 1) < V_R. \tag{16}$$

At this stage, it is convenient to transform (14) in the frequency-wavenumber domain,

$$k = \frac{\tau}{s}\omega + \frac{2\pi m'}{s} = \left(\frac{2\pi}{c_{pe}} - \frac{2\pi n}{f_e s}\right)f + \frac{2\pi m'}{s}. \tag{17}$$

This form is advantageous as it explicitly contains the frequency, which can be set to $f = f_e$. In the frequency-wavenumber domain, the excitation beams appear simply as straight lines of equal and positive slope, see Figure 7.

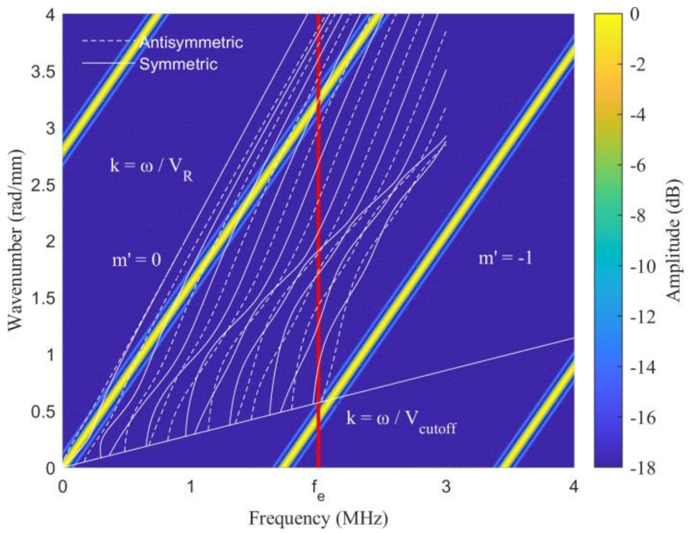

Figure 7. Excitation spectrum $\boldsymbol{H}_+$ in the frequency-wavenumber domain for a 32-element array with pitch 2.25 mm and target mode at $(\boldsymbol{f_e}, \boldsymbol{c_{pe}})$. The excitation beams appear as straight lines. The excitation beam for $\boldsymbol{m'} = \mathbf{0}$ intersects the frequency spectrum (in red) on top of $\boldsymbol{S3}$ mode at 2 MHz. The white lines represent dispersion curves of a 10 mm thick aluminium sample.

Condition (15) reads

$$\frac{\omega_e}{V_{cutoff}} > \left(\frac{2\pi}{\lambda_e} - \frac{2\pi n}{s}\right) + \frac{2\pi(n-1)}{s} \Rightarrow s < \frac{\lambda_e}{1-\frac{V_{phase}}{V_{cutoff}}}. \tag{18}$$

Similarly, condition (16) is stated as

$$\frac{\omega_e}{V_R} < \left(\frac{2\pi}{\lambda_e} - \frac{2\pi n}{s}\right) + \frac{2\pi(n+1)}{s} \Rightarrow s < \frac{\lambda_e}{\frac{V_{phase}}{V_R}-1}. \tag{19}$$

Conditions (18) and (19) set an upper bound for the pitch. Exploiting the fact that $V_{cutoff} > V_{phase}$ and $V_R < V_{phase}$ for any guided wave mode, both conditions can be expressed in the more compact form $s < \min\left(\frac{\lambda_e}{1-\epsilon_1}, \frac{\lambda_e}{\epsilon_2}\right)$, where ϵ_1, ϵ_2 are positive numbers such that $V_{phase}/V_{cutoff} = \epsilon_1$ and $V_{phase}/V_R = 1 + \epsilon_2$. As an example, consider an array on top of a 10 mm aluminium plate operating at 2 MHz with target mode S3. Then, $\epsilon_1 = 0.17, \epsilon_2 = 0.25,\ \lambda_e = 1.88$ mm, and simple calculations yield

$$\min\left(\frac{\lambda_e}{1-\epsilon_1}, \frac{\lambda_e}{\epsilon_2}\right) = \frac{\lambda_e}{1-\epsilon_1} = 2.27 \text{ mm}.$$

Condition (18) proved stricter than condition (19) at the scenario above. That is indeed the case when low dispersion modes close to the Rayleigh wave are targeted. Therefore, for the cases examined in this work, only condition (18) is significant.

The above conditions do not eliminate grating lobes in the backwards direction. For this purpose, H_- is examined. The grating lobes are located at

$$c_p = -\left(1 - \frac{m'\lambda}{s}\right)\frac{s}{\tau}. \tag{20}$$

In a similar manner, (20) is first transformed to

$$k = -\frac{\tau}{s}\omega + \frac{2\pi m'}{s} = -\left(\frac{1}{\lambda_e f_e} - \frac{n}{f_e s}\right)\omega + \frac{2\pi m'}{s}, \tag{21}$$

which shows that the excitation beams related to backward propagation are also straight lines with equal but negative slope. Next, it is required that the excitation beam given by $m' = -n + 1$ does not intersect with the frequency spectrum inside the modal region, as shown in Figure 8 for a 128-element, 0.75 mm pitch array with time delay set to $\tau = s/c_{pe}$, to enhance the forward propagation of mode (f_e, c_{pe}).

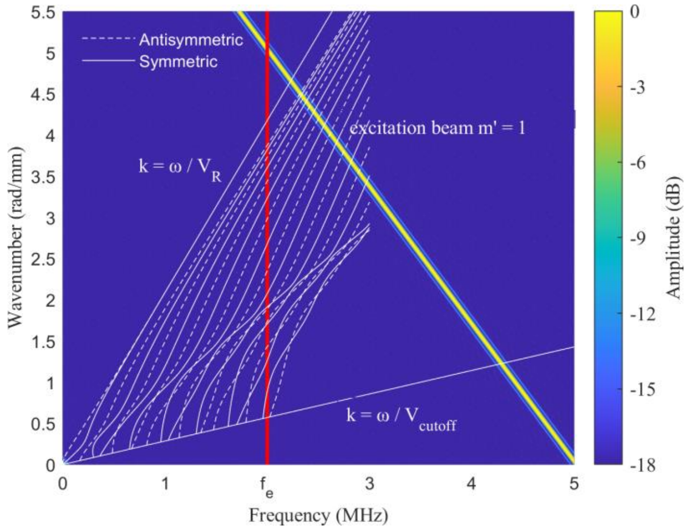

Figure 8. Excitation spectrum $\boldsymbol{H_{-}}$ in the frequency-wavenumber domain for a 128-element array with pitch 0.75 mm and target mode at $\left(\boldsymbol{f_e}, \boldsymbol{c_{pe}}\right)$. Unidirectional propagation requires that the excitation beam for $\boldsymbol{m' = 1}$ does not intersect the frequency spectrum (in red) inside the excitable region, defined by the Rayleigh wave and cutoff lines. The white lines represent dispersion curves of a 10 mm thick aluminium sample.

This is ensured if the excitation beam assumes a higher wavenumber value that the Rayleigh wave mode at $f = f_e$,

$$\frac{\omega_e}{V_R} < -\left(\frac{2\pi}{\lambda_e} - \frac{2\pi n}{s}\right) + \frac{2\pi(-n+1)}{s} \Rightarrow s < \frac{\lambda_e}{1+\frac{V_{\text{phase}}}{V_R}}. \tag{22}$$

In contrast to condition (18) the above condition not only necessary, but also sufficient. In other words, if it is satisfied, unidirectional propagation is enforced. Furthermore, if $V_{\text{phase}} \approx V_R$ the condition becomes $s < \frac{\lambda_e}{2}$, which is a well-known condition applied in phased array beam steering [39]. Note that this condition is related only to the unidirectionality of the mode and not to propagation in the forward direction.

Although conditions (18) and (22) were derived in a systematic way, some assumptions were made. Specifically, the whole derivation is solely based on the excitation spectrum, completely neglecting the effect of the single element response. In a sense, it is assumed that the single element distributes energy uniformly across the modes, while in fact, more energy is distributed to the low wavenumber modes. Furthermore, the excitation beams and frequency spectrum are simply treated as lines with zero bandwidth. For these reasons, in practice, these conditions are expected to be slightly violated.

3.3 Apodisation

Apodisation profiles can be employed to potentially improve guided wave excitation. Standard apodisation windows such as Hanning or Blackman eliminate the side lobes but increase the width of the main lobe [29]. In this section, an apodisation profile is derived based on an optimisation process. The apodisation function is compared with common apodisation profiles in Section 4.3.

Consider the general form (6) of the spectrum H_{+}. First, the terms that do not depend on frequency or wavenumber are omitted. The modified spectrum is given by $\overline{H} = \sum_{r=0}^{N-1}\sum_{q=0}^{r-1} A_r A_q \cos\big((ks - \omega\tau)(r-q)\big)$, which can be expressed in the more compact form

$$\overline{H} = \underline{A}^T \widehat{H} \underline{A},$$

where $\underline{A} = (A_0, \dots, A_{N-1})^T$ and $\widehat{H}$ is a $N \times N$ matrix with elements

$$[\widehat{H}_{rq}] = \begin{cases} cos\big((ks - \omega\tau)(r-q)\big), q < r \\ 0, \ otherwise \end{cases}$$

where $r, q = 0, \dots, N-1$. Next, an objective function that needs to be maximised is defined [10,40]

$$\Delta = \frac{\underline{A}^T \widehat{H}_e \underline{A}}{\underline{A}^T \widehat{H}_s \underline{A}}, \tag{23}$$

where $\widehat{H}_e = \sum_{p=0}^{P} \widehat{H}_{ep}(f_{ep}, k_{ep})$ and $\widehat{H}_s = \sum_{p'=0}^{P'} \widehat{H}_{sp'}(f_{sp'}, k_{sp'})$. The points in the frequency-wavenumber domain (f_{ep}, k_{ep}), $(f_{sp'}, k_{sp'})$ correspond to modes to enhance and suppress, respectively. The critical points of Δ are found by imposing the requirement

$$\partial_{A_r} \Delta = 0 \Rightarrow \left(\widehat{H}_e + \widehat{\mathrm{H}}_{\mathrm{e}}^{\mathrm{T}} - \lambda\left(\widehat{H}_s + \widehat{\mathrm{H}}_{\mathrm{s}}^{\mathrm{T}}\right)\right)\underline{A} = 0 \Rightarrow R\underline{A} = \lambda\underline{A}, \tag{24}$$

where $R = \left(\widehat{H}_s + \widehat{\mathrm{H}}_{\mathrm{s}}^{\mathrm{T}}\right)^{-1}\left(\widehat{H}_e + \widehat{\mathrm{H}}_{\mathrm{e}}^{\mathrm{T}}\right)$. Solution of (24) results in finding the eigenvalues and eigenvectors of R, which in the case examined in Section 4.3 was an invertible matrix. The apodisation profile is selected as the eigenvector $\underline{A}_{\mathrm{opt}}$ which corresponds to the largest eigenvalue λ_{max}.

4. Experimental results

The experimental setup is presented in Figure 9. Two linear 2.25 MHz Vermon arrays with 128 elements and a pitch of 0.75 mm were used in pitch-catch configuration on top of a 10 mm thick 6082-T6 aluminium plate. FMC data was collected along an overall line scan of 192 mm by using each element of the receiver probe as independent receivers. The length of the phased array probe is 96mm so the 192mm line-scan was captured in two steps (2x96 mm) by manually moving the probe. The separation distance was set in the first capture approximately to 200 mm edge-to-edge. The transducers were aligned with a metallic frame (not shown in Figure 9). The signals were generated and received with the 32Tx/32Rx/128E FI Toolbox [41], which is an array driver capable of producing arbitrary waveform signals using pulse width modulation with a 3-state pulser and digitising signals with a sampling frequency of 50 MHz. To excite a single mode, a narrowband signal was required. For that reason, in all following results, the excitation was a 14-cycle Hanning windowed toneburst centred at 2 MHz, leading to 20MHz·mm operating frequency-thickness product. The excitation signal was Hanning windowed to suppress any sidelobes [15]. The selected number of cycles narrows the frequency band of the signal approximately to 0.17 MHz at -6 dB. Although this is desired to excite a single mode, an immediate downside is the decrease in spatial resolution of the travelling wave, as the length of the wave-packet increases. However, the wavelengths of the guided wave modes at 20 MHz·mm are in the range $1.5 - 3$ mm for the low dispersion modes, say $A1 - S5$. This can compensate for the high number of cycles. All 2DFFT [42] results are presented on top of the dispersion curves (in white) for the 10 mm thick aluminium sample that was used for the experiments.

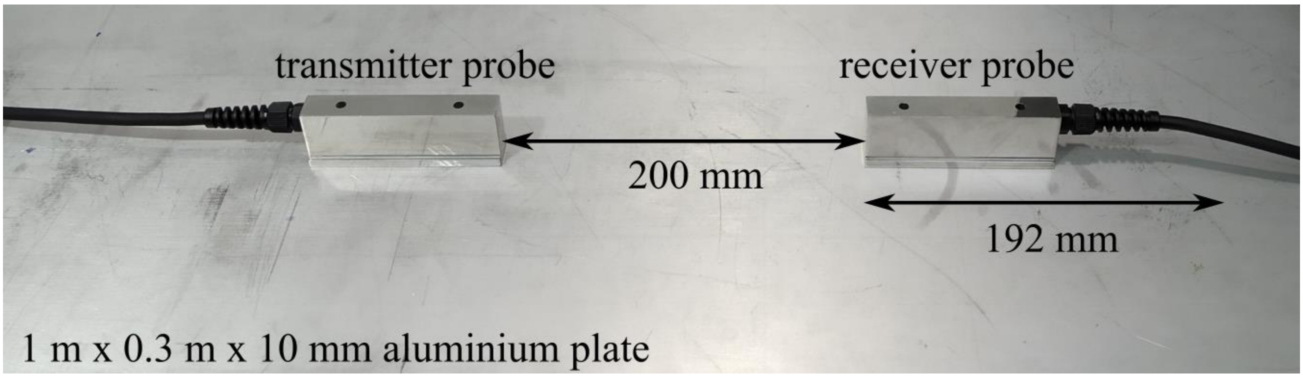

Figure 9. Experimental setup, showing two linear 2.25 MHz arrays with 128 elements operating in pitch-catch technique on top of a 10 mm aluminium plate.

All signals were reconstructed synthetically [43,44]. More specifically, given the full matrix of signals $[s_{rq}(t)]$, where index r and q denote the transmitting and receiving elements, respectively, the linearity of (3) suggests the reconstructed signal at x_q is given by

$$u(x_q, h, t) = \sum_{r=0}^{N-1} A_r s_{rq}(t - t_r).$$

This means once the full matrix is obtained, any delay law and apodisation profile can be constructed synthetically. In this work, only linear time delays are considered; however, general voltage amplitudes A_r are addressed in Section 4.3.

The 2DFFT of a single element of the array is shown in Figure 10. Considering the amplitude decomposition (7), this plot is related to term A_S. Essentially, the single element response sets an amplitude floor, which is then enhanced or suppressed by the excitation spectrum. Simple examination reveals more energy is placed at the low wavenumber modes, which are in general more dispersive, such as $A8$ and $S8$, while little energy is distributed to higher wavenumber modes, such as $A1$ and $S1$. The 2DFFT map reveals that there is an offset between the experimental data and the dispersion curves, especially for high wavenumber modes. This error is expected to be related to the frequency-wavenumber discretisation involved in the 2DFFT [45]. The numerical error was found around 3% and did not raise any issues, thus was deemed acceptable for the purposes of this work.

In the experimental results that follow, mode $S3$ at $(f_e, k_e) = (2\text{ MHz}, 3.34\text{ rad/mm})$ was targeted. Based on the excitability function presented in Figure 2b, $S3$ is more excitable that any lower order mode at 20 MHz·mm. Furthermore, this mode is less dispersive compared to higher order modes such as $A5, S5, A6, \cdots$,A9. Modes $A4$ and $S4$ exhibit also low dispersion behavior and good excitability. However, mode $S3$ was preferred due to its lower wavelength at 2 MHz, namely 1.89 mm, over 2.03 and 2.21 mm of $A4$ and $S4$, respectively. These modes are also considered in Section 4.3. In all that follows, modes $S3, A4$ and $S4$ were excited using (9) with $n = 0$.

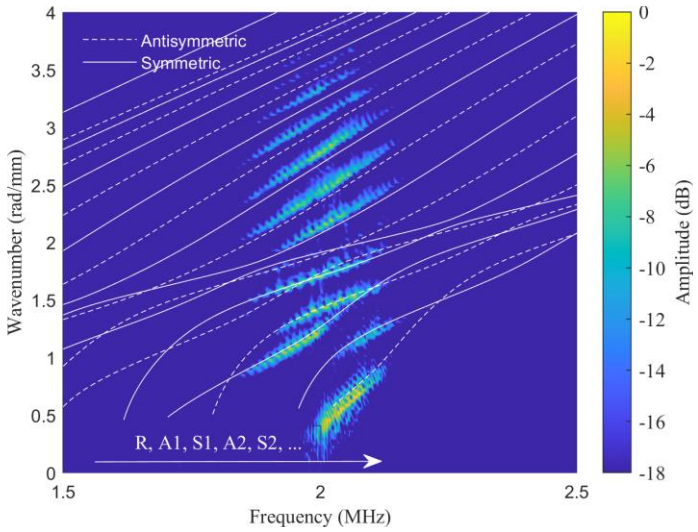

Figure 10. 2DFFT of a single element for a 14-cycle Hanning windowed toneburst centred at 2 MHz. More energy is distributed to the low wavenumber modes.

4.1 Experimental investigation of the influence of the excitation spectrum's bandwidth to single mode excitation

Three setups are presented, varying the number of elements of the transmitter array, to investigate experimentally the effect of the excitation spectrum's bandwidth on guided wave excitation. In all setups, uniform amplitudes $A_r = 1$ and time delay constant $\tau = 200$ ns were employed. The excitation bandwidth as given in Table 1 is plotted in red on top of the 2DFFT results presented in Figure 11a, b and c. In the first configuration, only the first 32 elements of the transmitter array were used. As shown in Figure 11a, a significant amount of energy is distributed not only to $S3$ but also its neighbours, namely modes $A3$ and $A4$. This is expected, as the excitation bandwidth associated with a 32-element array is large enough to significantly overlap with $A3$ and $A4$ around 2 MHz. In the second configuration, the first 64 elements were used for the excitation. Energy leakage is reduced, and more energy is focused on mode $S3$, see Figure 11b. This is due to the narrower spectrum bandwidth of a 64-element array. Finally, the excitation is further improved utilising all 128 elements and can be considered as single mode. The A-scans for the three configurations examined are shown in Figure 12. The signals shown in Figure 12a, b and c were captured at a distance around 303, 307 and 320 mm away from the first element of the transmitter array, respectively. This way, the peak amplitude of S3 occurs around 122 μs for all three cases. The group velocity of $A3, S3$ and $A4$ was found to be 2.77 m/ms, 2.62 m/ms and 2.45 m/ms, respectively, with error less than 0.5%, 0.5% and 1.3% compared with the theoretical group velocities obtained from the Dispersion Calculator [46].

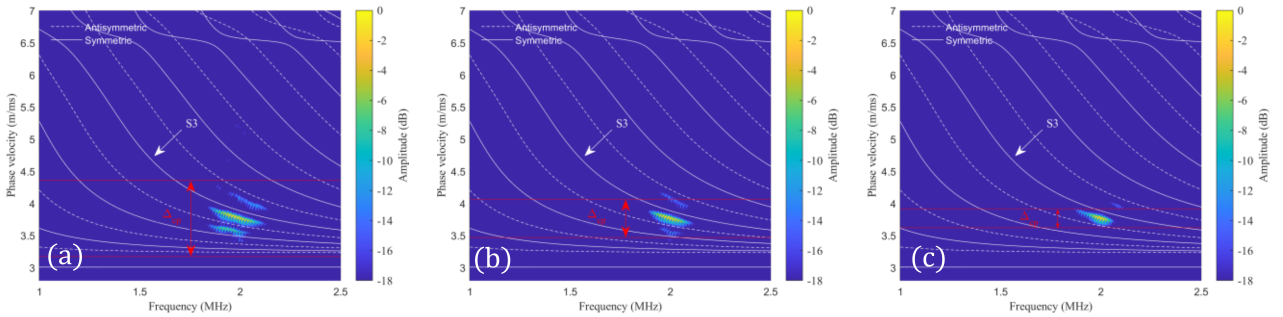

Figure 11. 2DFFT produced with 0.75 mm pitch array and a) 32, b) 64 and c) 128 elements. The response improves significantly with the increase of number of elements, which narrows the bandwidth of the excitation spectrum.

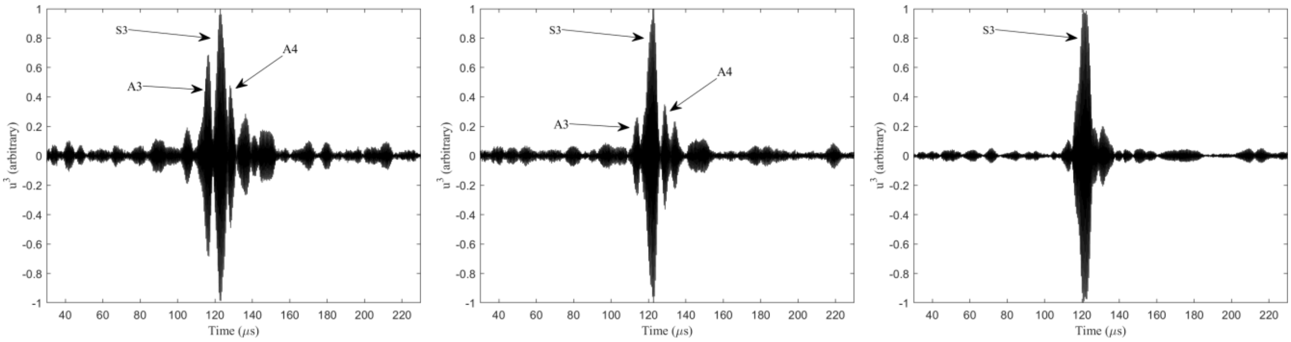

Figure 12. Example A-scans targeting mode S3 varying the number of elements a) 32 elements were used, modes A3 and A4 are present. b) 64 elements were used, modes A3 and A4 are suppressed c) 128 elements were used, mode S3 is dominant.

4.2 Experimental verification of the generation of grating lobes

Another set of experiments was conducted to examine the validity of conditions (18) and (22), which read $s < 2.27$ mm and $s < 0.84$ mm, respectively.

The 2DFFT in the forward direction for $s = 1.5, 2.25$ and 3 mm is shown in Figure 13a, b and c. The data was obtained from the same FMC dataset by skipping one, two and three elements of the transmitter array. The active aperture was kept constant at 96 mm, and voltage amplitudes were uniform. For $s = 1.5$ mm, condition (18) is satisfied and a single mode is generated in the forward direction, see Figure 13a. The response is very similar to the one presented in Figure 11c. However, for $s = 2.25$ mm, an unwanted mode is generated, as shown in Figure 13b. The location of the unwanted mode is at the intersection of the frequency spectrum with an excitation beam (grating lobe), which can be found substituting $m' = -1$ in (17). This means condition (18) is violated somewhat earlier in practice, which is expected, as both the frequency and the excitation beams are associated with finite bandwidths. The effect of the $m' = -1$ beam is present also for $s = 3$ mm, as shown in Figure 13c. The increase of the pitch has shifted the beam to the left, thus compared to the previous case, a higher wavenumber unwanted mode is generated.

Next, the 2DFFT for guided wave propagation in the backward direction is presented in Figure 13d, e and f, for $s = 1.5,\ 2.25$ and 3 mm, respectively. This time, the time delay law applied synthetically is given by $t_r = (N - 1 - r)\tau$, to mimic a beam propagating in the $-x$ direction. In what follows, the 0 dB value corresponds to the maximum amplitude of the forward propagating wave. For example, the 0 dB value in Figure 13d corresponds to the maximum amplitude of Figure 13a. Note that for $s = 0.75$ mm condition (19) is satisfied and no energy higher than -18 dB was found to propagate in the backwards direction, thus this result is not presented. For all three setups, condition (19) is violated and unwanted modes propagate. These are located at the intersection between the frequency spectrum and the excitation beams given by (21). Specifically, Figure 13 d, e and f show the propagating modes on top of the excitation beams for $m' = 1,\ m' = 2$ and $m' = 2,3$, respectively. The above results are in striking agreement with the material developed in Section 3.2.

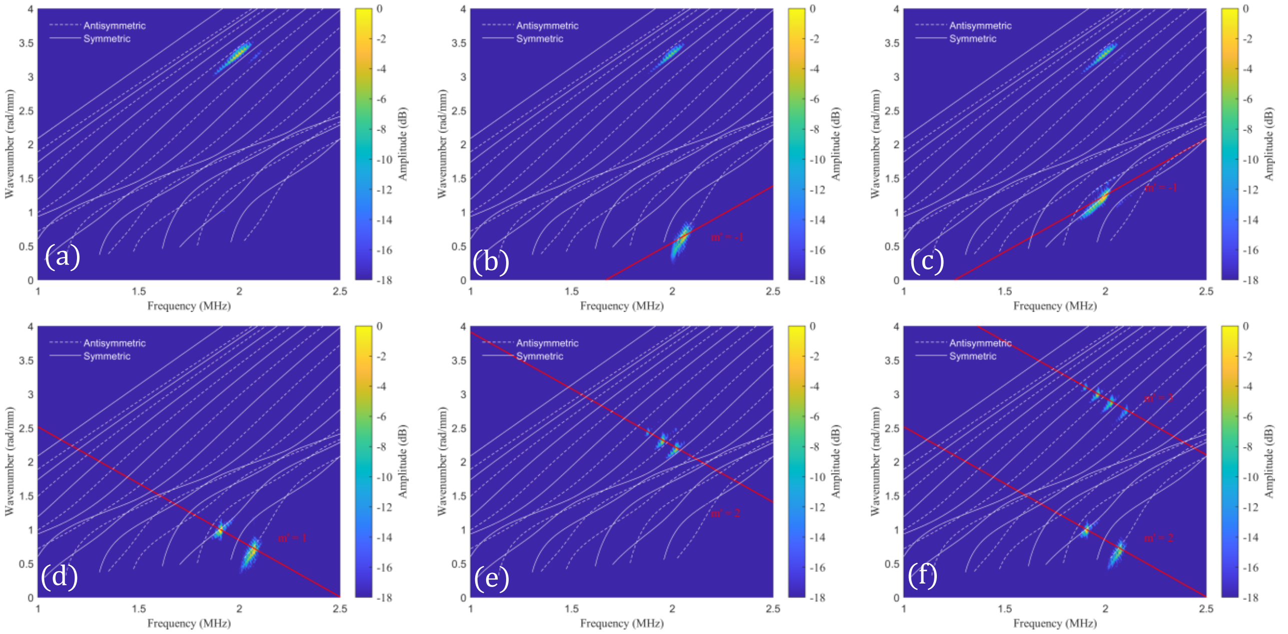

Figure 13. *Top Row*: 2DFFT in the forward direction, varying the pitch value; red line indicates an excitation beam. a) $\boldsymbol{s = 1.5}$ mm. No excitation beams intersect with the frequency spectrum and only $\boldsymbol{S3}$ is excited. b) $\boldsymbol{s = 2.25}$ mm. The excitation beam for $\boldsymbol{m' = -1}$ intersects with the frequency spectrum, generating low wavenumber modes. c) $\boldsymbol{s = 3}$ mm. The same beam is activated. This time, the beam is shifted to the left, resulting in excitation of a higher wavenumber mode. *Bottom Row*: 2DFFT in the backward direction, varying the pitch value. d) $\boldsymbol{s = 1.5}$ mm. The excitation beam for $\boldsymbol{m' = 1}$ intersects with the frequency spectrum. e) $\boldsymbol{s = 2.25}$ mm. Although the excitation beam for $\boldsymbol{m' = 1}$ beam does not activate any modes, the beam for $\boldsymbol{m' = 2}$ does. f) $\boldsymbol{s = 3}$ mm. Two excitation beams intersect with the frequency spectrum inside the modal region, leading to the excitation of lower and higher wavenumber modes.

Similar results can be obtained if the elements of the array are grouped to simulate larger elements. For example, instead of skipping two elements, the array can be partitioned into groups of three elements, combining $1 - 3, 4 - 6, \dots, 124 - 126$. The two approaches are equivalent in the sense that both give the same pitch value. However, the response of a single group is different from the single element response shown in Figure 10, due to the larger width of the group. The 2DFFT of a group that consists of three elements is shown in Figure 14. The energy distribution to the higher wavenumber modes is below -18 dB. This makes targeting these modes more challenging, mainly for three reasons. First, even if condition (18) is satisfied and no grating lobes are present, a small amount of energy may still be distributed to low wavenumber modes, as the group element response enhances these modes significantly. Second, the energy of the high wavenumber targeted mode is decreased compared to the case where the elements are not grouped, leading to lower signal to noise ratio. Comparison of the 2DFFT result shown in Figure 15a with Figure 11c revealed that the amplitude of $S3$ was 10 time lower. Finally, if condition (18) is violated, the unwanted modes are expected to dominate the signal.

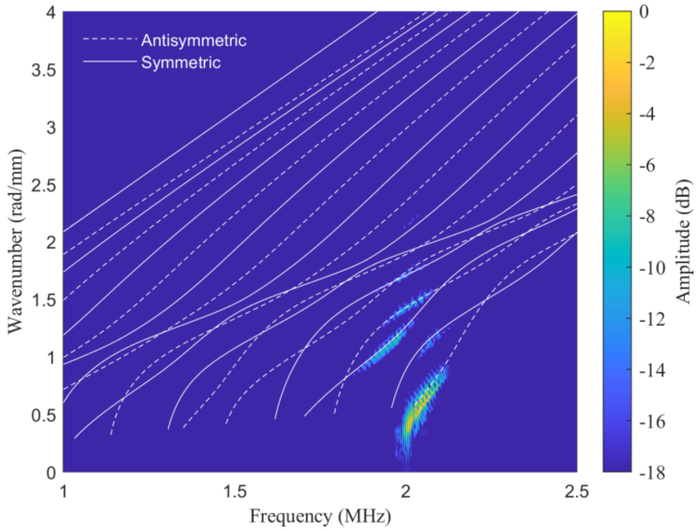

Figure 14. 2DFFT of a group of 3 elements. More energy is distributed to the low wavenumber modes.

Figure 15a, b and c present 2DFFT results in the forward direction grouping two, three and four elements, respectively. All remaining parameters were kept identical to the results already presented in Section 4.2. The 2DFFT for pitch value 1.5 mm is shown in Figure 15a. Similar to Figure 13a, most of the energy is focused on $S3$. However, in this case, energy leakage towards low wavenumber modes is present. Figure 15b and c correspond to pitch values of 2.25 and 3 mm. Again, these are similar to Figure 13b and c, but with a sharp difference. Specifically, the energy of the targeted mode $S3$ is significantly lower compared to energy level of the unwanted modes, which dominate wave propagation, being approximately 18 dB higher than S3. This is expected, as the single group response amplifies low wavenumber modes, see Figure 14. The results for propagation in the $-x$ direction are very similar to the ones already presented in Figure 13d, e and f thus are not repeated here.

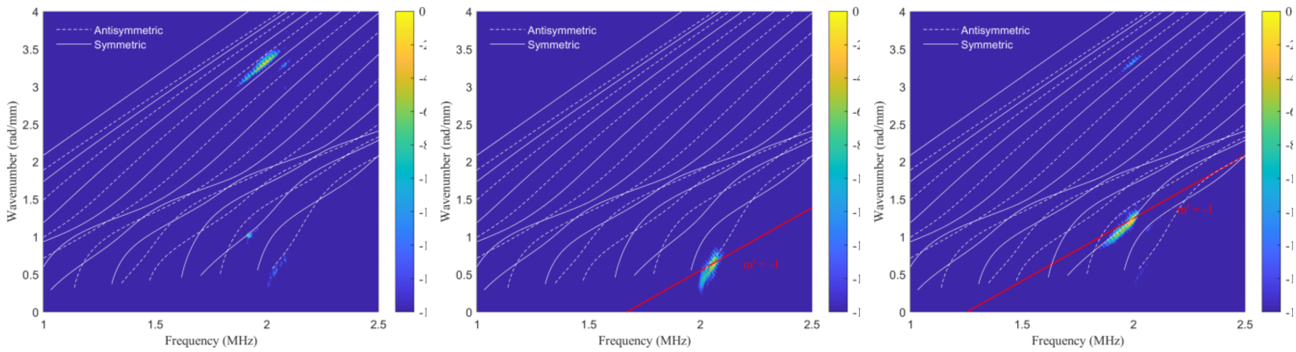

Figure 15. 2DFFT in the forward direction, varying the pitch value; red line indicates an excitation beam. a) $\boldsymbol{s = 1.5}$ mm. Mode S3 is dominant. b) $\boldsymbol{s = 2.25}$ mm. The excitation beam for $\boldsymbol{m' = -1}$ intersects with the frequency spectrum, generating low wavenumber modes. Mode S3 is below -18 dB. c) s=3 mm. The same beam is activated. Mode S3 is approximately 18 dB lower.

4.3 Experimental assessment of apodisation

The experimental results presented so far assume uniform voltage amplitudes across the elements of the array. This raises a natural question, whether an apodisation profile can improve the purity of the targeted mode.

Here, three apodisation profiles are compared, namely uniform, Blackman window and the optimised, as shown in Figure 16a. The optimised profile is the result of the optimisation problem described in Subsection 3.3, where the points in the frequency-wavenumber domain to enhance and suppress are manually selected based on Figure 11c. In general, the definition of a suitable objective function is a subtle issue; different apodisation profiles result from different definitions. Here, the points to enhance and suppress are the points of maximum amplitude of $S3$ and $A4$, which in the frequency-phase velocity domain are given by $(f_{e,}\, c_{pe})$ and $\left(f_s, c_{ps}\right) = (2.08\text{ MHz}, 3.956\text{ m/ms})$. The effect of each of the three profiles on the phase velocity spectrum gated at 2 MHz is shown in Figure 16b, similar to Figure 4b but plotted in dB scale. As expected, the Blackman window significantly reduces the amplitude of the side lobes; however, the width of the main lobe increases. On the contrary, the optimised profile's spectrum is very similar to the uniform spectrum, with one key difference: the second side lobe's amplitude is significantly reduced. The peak of this side lobe is at $c_p = 3.959$ m/ms, which is very close to c_{ps}. The amplitude of $A4$ at $\left(f_s, c_{ps}\right)$ depends on the magnitude of the excitation spectrum at the same point. This means that the second side lobe is primarily responsible for the generation of $A4$, and it is exactly the same lobe that is suppressed by the optimised apodisation profile. Therefore, by reducing the magnitude of the second side lobe of the spectrum, the amplitude $A4$ is expected to decrease.

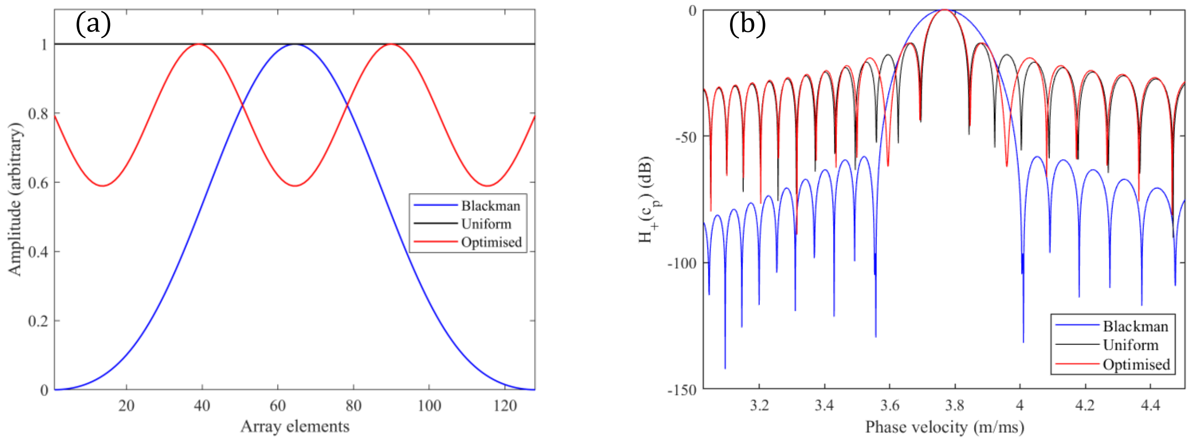

Figure 16. a) Uniform, Blackman and optimised apodisation profiles for 128-element array. b) The excitation spectrum for each of these profiles is shown. The response of the optimised and uniform profiles is very similar, but the second side's lobe amplitude is significantly reduced for the optimised profile, which is beneficial to enhance the purity of $\boldsymbol{S3}$.

The effect of the selected profiles on guided wave excitation is further investigated. Specifically, an experimental 2DFFT for each amplitude profile is computed and shown in Figure 17. The overall improvement is visible in the 2DFFT graph.

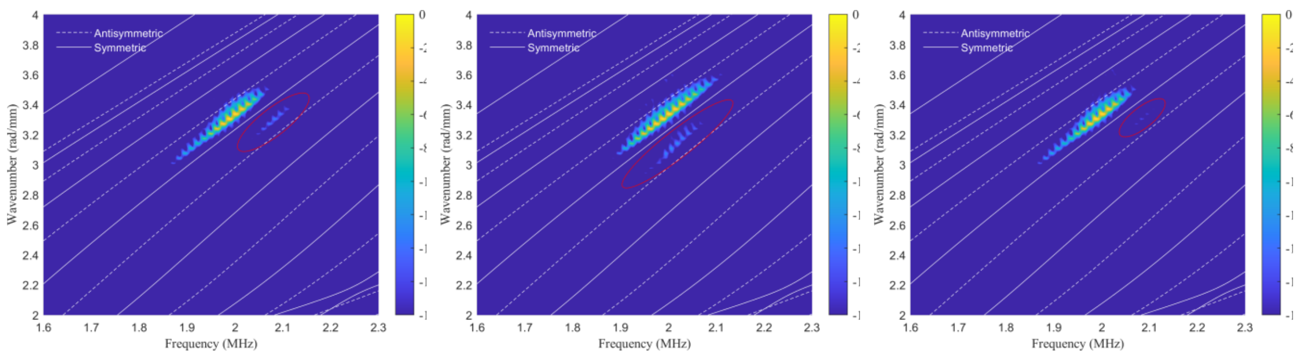

Figure 17. 2DFFT results for different apodisation profiles. The unwanted modes are encircled in red. a) Uniform amplitudes. The presence of A4 is not significant but visible. b) Blackman window. The presence of the unwanted mode is amplified. c) Optimised profile. A4 is suppressed.

The performance of each profile is further measured with the definition of an objective function which is similar to (23), defined by

$$\Delta^E = \frac{\sum_{p=0}^{3} A^E(f_{ep},k_{ep})}{\sum_{p'=0}^{14} A^E(f_{sp'},k_{sp'})},$$

but in this case $A^E(f_{ep},k_{ep})$, $A^E(f_{sp'},k_{sp'})$ represent amplitudes extracted directly from experimental 2DFFT results. For this calculation, four points of $S3$ and fifteen points of $A4$ were selected around 2 MHz. Then, the amplitude (linear scale) of these points was extracted from the 2DFFT for the cases of uniform, Blackman and optimised apodisation profiles. The experimental objective function together with its numerator and denominator is shown in Figure 18. The amplitude of the target mode for uniform amplitudes excitation was set to one and all others were scaled accordingly. As expected, the optimised apodisation profile performs better among the selected three, suggesting it is the most appropriate choice for single mode excitation.

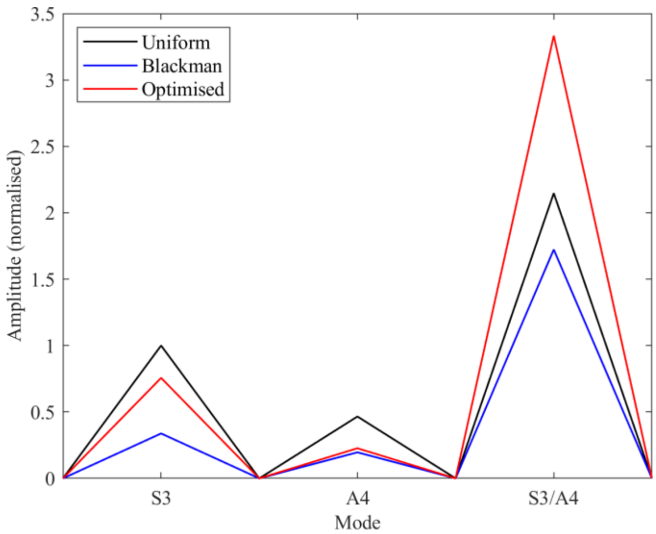

Figure 18. Amplitude comparison between Uniform, Blackman and Optimised profiles.

Next, the possibility of further improving single mode excitation using apodisation is investigated for more higher order modes, namely $A4$ and $S4$.

Figure 19 displays 2DFFT maps in the frequency-wavenumber domain. Uniform voltage amplitudes were employed. At 2 MHz, the wavenumber values of $A4$ and $S4$ read 3.109 rad/mm and 2.814 rad/mm, thus the required time delay constant is 185 ns and 167 ns, respectively. However, since the sampling period is 20 ns, the applied time delays need to be rounded to the closest multiple of 20, leading to 180 ns and 160 ns. This introduces an error of 5 ns and 7 ns. To bypass this issue, the excitation frequency for mode $A4$ was shifted to 1.94MHz. This way, energy is centered at $(f_{A4}, k_{A4}) = (1.94\ MHz, 2.95\ rad/mm)$, as shown Figure 19a. Targeting this point requires a time delay constant $\tau_{A4} \approx 180ns$. Most of the energy is focused on $A4$, while some energy leakage is observed to modes $S4$ and $S5$. A similar frequency shift may be employed to excite $S4$ at 160 ns. However, to illustrate the effect of applying a time delay law slightly different from the nominal one, mode $S4$ was excited at 2MHz. The maximum energy was found at point $(f_{S4}, k_{S4}) = (1.93MHz, 2.58\ rad/mm)$, see Figure 19b. Although the target mode is excited, in this case, mode $A5$ is significantly excited, spanning a wide range of frequencies, from 1.95 to 2.15 MHz.

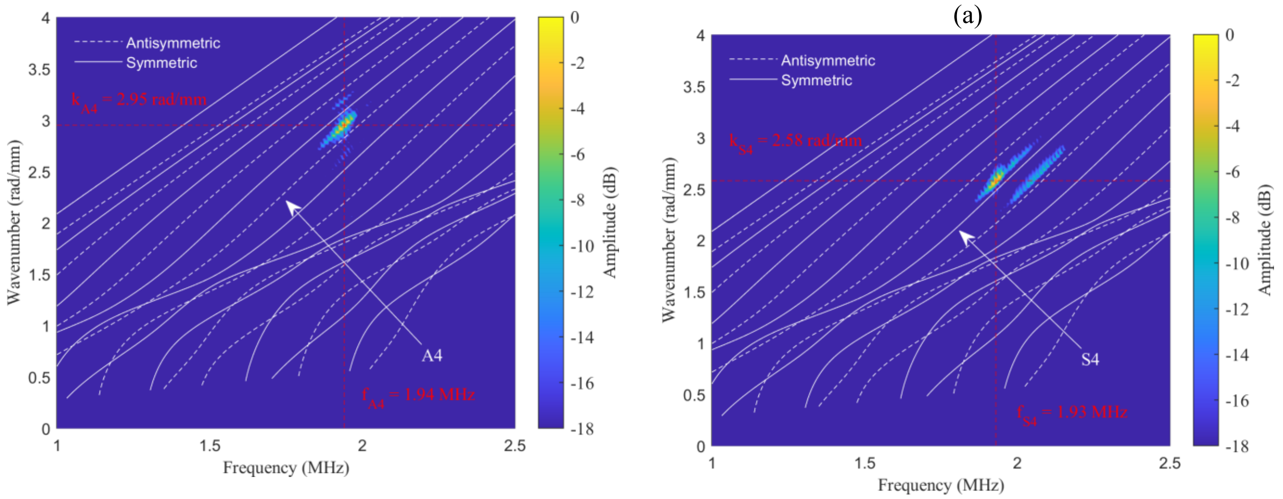

Figure 19. 2DFFT in frequency-phase velocity domain using uniform amplitudes and targeting modes a) A4, and b) S4.

The performance of uniform, Blackman and optimised profiles is tested on the selected modes. The optimised profile for mode $A4$ is shown in Figure 20a. An objective function according to (23) was defined. The point to enhance was selected as the point of maximum amplitude of $A4$. The points to suppress were selected as the maxima points of the first three side lobes of the excitation spectrum at 1.94 MHz. Figure 20b shows the optimised profile for mode $S4$. Again, the point to enhance was selected as the point of maximum amplitude of the targeted mode. The maxima of the first five side lobes at the same frequency were suppressed. These maxima occur at $c_p = 4.88, 5.01, 5.15, 5.30, 5.46$ m/ms. All these side lobes contribute to the excitation of the unwanted mode $A5$, as it spans a phase velocity range, from 4.7 to 5.4 m/ms. In this case, the Blackman window is expected to yield satisfactory results, as it effectively suppresses all side lobes.

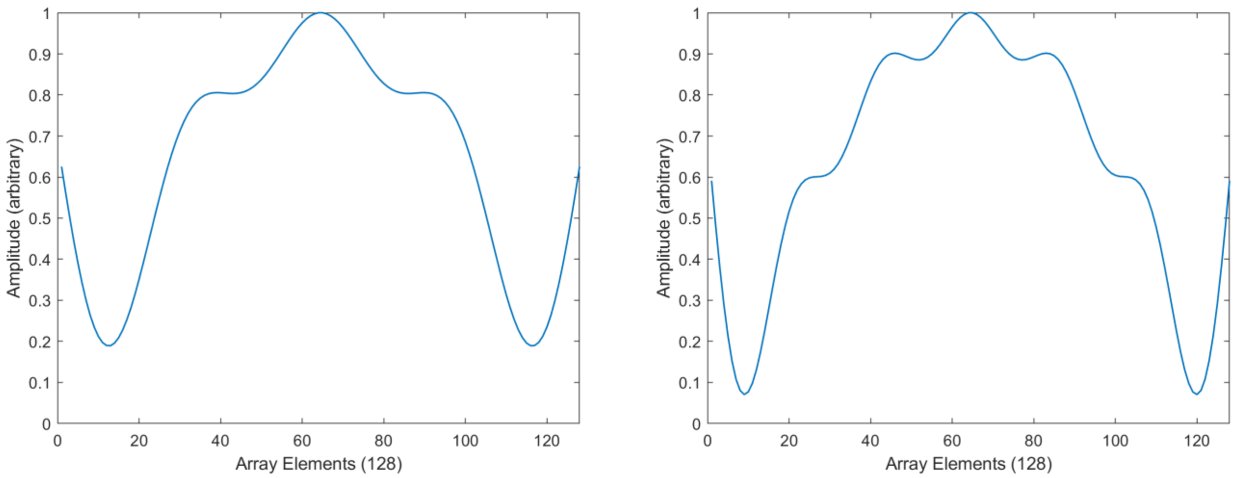

Figure 20. Optimised apodisation profile for A4 and S4 modes. a) A4 apodisation profile, b) S4 apodisation profile.

Figure 21a, b and c present 2DFFT results for uniform, Blackman and optimised apodisation profiles when the target mode is $A4$. Visual examination reveals that the optimised profile performs best, see Figure 21c, while the uniform and Blackman window have similar behavior. However, this is not true when targeting mode $S4$, see Figure 21d, e and f. In this case, the Blackman window yields better results, as shown in Figure 21e. This is not surprising, as the Blackman window suppresses all side lobes, and in this case, multiple sidelobes contribute to the generation of A5. The amplitude of the relevant modes extracted from the 2DFFT graphs is shown in Figure 22. The procedure followed was similar to the one described for Figure 18. Specifically, eight points along *A*4 and fifteen points along *S*4 and *S*5 around 1.94 MHz were selected for Figure 22a, while seven point along S4 and seventeen points along *A*5 around 1.93 MHz were selected to produce Figure 22b. The results agree with the previous visual observations.

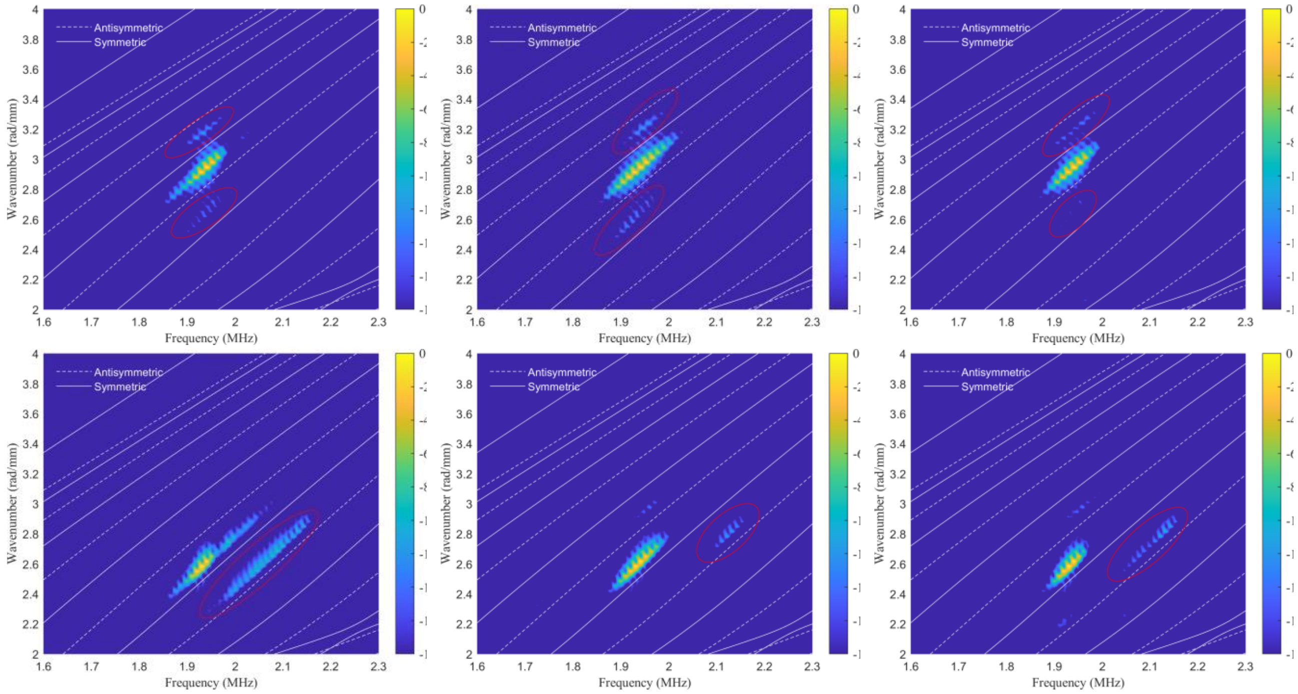

Figure 21. 2DFFT results for different apodisation profiles. Top Row (A4): a) Uniform amplitudes. b) Blackman window. c) Optimised profile. Bottom Row (S4): a) Uniform amplitudes. b) Blackman window. c) Optimised profile.

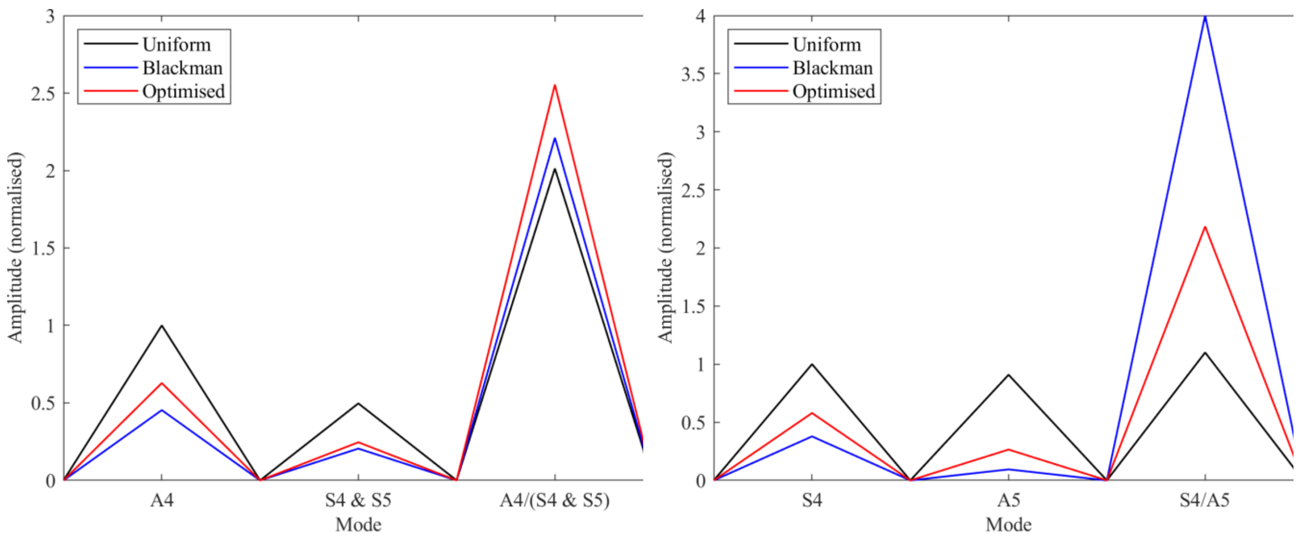

Figure 22 Amplitude comparison between Uniform, Blackman and Optimised profiles. a) Mode A4 is targeted. b) Mode S4 is targeted.

5. Conclusion

This study focused on the proper selection of key parameters for single mode excitation in the higher order mode region with a conventional linear array. An analytical model based on modal analysis was derived, showing the feasibility of the method even for guided wave related problems. An important decomposition between the excitation spectrum and the response of a single element was made. Then, a set of conditions was derived, see Table 2. These can be seen as guidelines for the proper selection of the number of elements, pitch and apodisation profile. The first condition determines the phase velocity bandwidth, and provided a pitch decides the number of elements. The second and third conditions are related to eliminating grating lobes in the forward and backward direction, respectively. Violation of the second condition will lead to propagation of unwanted modes, since a grating lobe will intersect with the frequency spectrum, generating low wavenumber modes. However, satisfaction of the same requirement does not ensure single mode excitation; for example, unwanted neighbouring modes might be generated, due to the small aperture length of the array. This means this condition is only necessary. On the contrary, the third condition is also sufficient, since it ensures unidirectional propagation. This condition is stricter that the necessary condition, in the sense that if it is satisfied, the necessary condition is satisfied as well. Therefore, it can be used to determine the pitch of the array. More specifically, the pitch should be small enough to satisfy this requirement, but large enough to increase the total length of array and thus decrease the excitation spectrum's bandwidth. Finally, the apodisation profile was optimised to possibly enhance the purity of the targeted mode. The exact form of the objective function is defined online, after performing 2DFFT analysis. This can be seen as a calibration process, tuning each voltage amplitude to improve guided wave excitation and propagation.

An experimental FMC dataset was obtained, to validate the above theoretical results. This allowed different number of elements and pitch values to be evaluated after post processing from the same raw data signals. The agreement between theoretical and experimental results was strong. Emphasis was placed on exciting $S3$, although modes $A4$ and $S4$ were targeted as well. The performance of different apodisation profiles was evaluated for each of these modes. The suitability of the apodised window depended on the energy distribution of the unwanted modes in the 2DFFT map. When they spanned a narrow frequency range, the optimised profile gave better results compared to the uniform amplitudes and Blackman window. However, when the unwanted mode spans a wider frequency range, multiple side lobes need to be suppressed. In this case, the Blackman window was found to perform best. The described setup integrated into a roller probe and its capability to excite a pure mode in the high frequency thickness product region could be a subject to be investigated in future work.

Table 2 Conditions for single mode excitation

Condition No.	Condition	Description
1	$N > \frac{2\lambda_e}{\Delta c_p^{m-s}} c_{pe}$	Suppression of neighbouring modes of targeted mode
2	$s < \frac{\lambda_e}{1 - \frac{V_{phase}}{V_{cutoff}}}$	No grating lobes in $+x$ direction
3	$s < \frac{\lambda_e}{1 + \frac{V_{\mathrm{phase}}}{V_R}}$	No grating lobes in $-x$ direction (unidirectional propagation)
4	$max(\Delta)$	Further enhancement of the purity of the targeted mode

Funding: This work was supported by the Advanced Nuclear Research Centre (ANRC).

References

[1] J. Chandrasekaran, I. Anto, K. Balasubramaniam, K.S. Venkataraman, Higher order modes cluster (HOMC) guided waves for online defect detection in annular plate region of above-ground storage tanks, Insight Non-Destructive Test. Cond. Monit. 51 (2009) 606–611. https://doi.org/10.1784/insi.2009.51.11.606.

[2] C. Jayaraman, C. V. Krishnamurthy, K. Balasubramaniam, Higher order modes cluster (HOMC) guided waves - A new technique for ndt inspection, in: AIP Conf. Proc., American Institute of Physics, 2009: pp. 121–128. https://doi.org/10.1063/1.3114094.

[3] J.P. Koduru, J.L. Rose, Mode controlled guided wave tomography using annular array transducers for SHM of water loaded plate like structures, Smart Mater. Struct. 22 (2013). https://doi.org/10.1088/0964-1726/22/12/125021.

[4] H. Kannajosyula, C.J. Lissenden, J.L. Rose, Analysis of annular phased array transducers for ultrasonic guided wave mode control, Smart Mater. Struct. 22 (2013). https://doi.org/10.1088/0964-1726/22/8/085019.

[5] H. Taheri, A.A. Hassen, Nondestructive ultrasonic inspection of composite materials: A comparative advantage of phased array ultrasonic, Appl. Sci. 9 (2019). https://doi.org/10.3390/app9081628.

[6] P. Cawley, D. Alleyne, The use of Lamb waves for the long range inspection of large structures, Ultrasonics. 34 (1996) 287–290. https://doi.org/10.1016/0041-624X(96)00024-8.

[7] J.L. Rose, Ultrasonic Guided Waves in Solid Media, Cambridge University Press, 2014.

[8] G. Veit, P. Bélanger, An ultrasonic guided wave excitation method at constant phase velocity using ultrasonic phased array probes, Ultrasonics. 102 (2020). https://doi.org/10.1016/j.ultras.2019.106039.

[9] J.L. Rose, P. Morrow, Y. Zhu, Ultrasonic Guided Wave Modal Analysis Technique (UMAT) for Defect Detection, in: Conf. Proc. Soc. Exp. Mech. Ser. , 2011.

[10] J.P. Koduru, S. Momeni, J.L. Rose, Phased annular array transducers for omnidirectional guided wave mode control in isotropic plate like structures, Smart Mater. Struct. 22 (2013). https://doi.org/10.1088/0964-1726/22/12/125022.

[11] B.C. Lee, W.J. Staszewski, Lamb wave propagation modelling for damage detection: I. Two-dimensional analysis, Smart Mater. Struct. 16 (2007) 249–259. https://doi.org/10.1088/0964-1726/16/2/003.

[12] M. Faisal Haider, M.Y. Bhuiyan, B. Poddar, B. Lin, V. Giurgiutiu, Analytical and experimental investigation of the interaction of Lamb waves in a stiffened aluminum plate with a horizontal crack at the root of the stiffener, J. Sound Vib. 431 (2018) 212–225. https://doi.org/10.1016/j.jsv.2018.06.018.

[13] R.S.C. Monkhouse, P.D. Wilcox, P. Cawley, Flexible interdigital PVDF transducers for the generation of Lamb waves in structures, Ultrasonics. 35 (1997) 489–498. https://doi.org/10.1016/S0041-624X(97)00070-X.

[14] A. Gachagan, G. Hayward, R. Banks, A flexible piezoelectric transducer design for efficient generation and reception of ultrasonic lamb waves, IEEE Trans. Ultrason. Ferroelectr. Freq. Control. 52 (2005) 1175–1182. https://doi.org/10.1109/TUFFC.2005.1504004.

[15] D.N. Alleyne, P. Cawley, Optimization of lamb wave inspection techniques, NDT E Int. 25 (1992) 11–22. https://doi.org/10.1016/0963-8695(92)90003-Y.

[16] S.H.K. Reddy, A. Vasudevan, P. Rajagopal, K. Balasubramaniam, Scattering of Higher Order Mode Clusters (HOMC) from surface breaking notches in plates with application to higher temperature gradients, NDT E Int. 120 (2021) 102441. https://doi.org/10.1016/j.ndteint.2021.102441.

[17] J. Chandrasekaran, C. V. Krishnamurthy, K. Balasubramaniam, Axial higher order modes cluster (A-HOMC) guided wave for pipe inspection, AIP Conf. Proc. 1211 (2010) 161–168. https://doi.org/10.1063/1.3362262.

[18] P. Khalili, P. Cawley, Excitation of Single-Mode Lamb Waves at High-Frequency-Thickness Products, IEEE Trans. Ultrason. Ferroelectr. Freq. Control. 63 (2016) 303–312. https://doi.org/10.1109/TUFFC.2015.2507443.

[19] Z. Abbasi, F. Honarvar, Contribution of Lamb wave modes in the formation of higher order modes cluster (HOMC) guided waves, Proc. Inst. Mech. Eng. Part C J. Mech. Eng. Sci. 236 (2022) 3595–3605. https://doi.org/10.1177/09544062211042410.

[20] P. Belanger, High order shear horizontal modes for minimum remnant thickness, Ultrasonics. 54 (2014) 1078–1087. https://doi.org/10.1016/j.ultras.2013.12.013.

[21] K. Shivaraj, K. Balasubramaniam, C. V. Krishnamurthy, R. Wadhwan, Ultrasonic circumferential guided wave for pitting-type corrosion imaging at inaccessible pipe-support locations, J. Press. Vessel Technol. Trans. ASME. 130 (2008) 0215021–12150211. https://doi.org/10.1115/1.2892031.

[22] P. Khalili, P. Cawley, The choice of ultrasonic inspection method for the detection of corrosion at inaccessible locations, NDT E Int. 99 (2018) 80–92. https://doi.org/10.1016/j.ndteint.2018.06.003.

[23] S.H.R. K, P. Rajagopal, K. Balasubramaniam, S. Hill, S. Dixon, Interaction of Higher Order Modes Cluster (HOMC) guided waves with notch-like defects in plates Interaction of Higher Order Modes Cluster (HOMC) Guided Waves with Notch-like Defects in Plates, 030015 (2017). https://doi.org/10.1063/1.4974583.

[24] S. Harsha, K. Reddy, A. Vasudevan, P. Rajagopal, K. Balasubramaniam, Scattering of Higher Order Mode Clusters (HOMC) from surface breaking notches in plates with application to higher temperature gradients, NDT E Int. 120 (2021) 102441. https://doi.org/10.1016/j.ndteint.2021.102441.

[25] M. Tabatabaeipour, O. Trushkevych, G. Dobie, R.S. Edwards, R. McMillan, C. Macleod, R. O'Leary, S. Dixon,

A. Gachagan, S.G. Pierce, Application of ultrasonic guided waves to robotic occupancy grid mapping, Mech. Syst. Signal Process. 163 (2022). https://doi.org/10.1016/j.ymssp.2021.108151.

[26] J.L. Rose, S.P. Pelts, M.J. Quarry, A comb transducer model for guided wave NDE, 1998.

[27] W. Zhu, J.L. Rose, Lamb wave generation and reception with time-delay periodic linear arrays: a BEM simulation and experimental study, IEEE Trans. Ultrason. Ferroelectr. Freq. Control. 46 (1999) 654–664. https://doi.org/10.1109/58.764852.

[28] J. Li, J.L. Rose, Implementing guided wave mode control by use of a phased transducer array, IEEE Trans. Ultrason. Ferroelectr. Freq. Control. 48 (2001) 761–768. https://doi.org/10.1109/58.920708.

[29] D. Cirtautas, V. Samaitis, L. Mažeika, R. Raišutis, E. Žukauskas, Selection of Higher Order Lamb Wave Mode for Assessment of Pipeline Corrosion, Metals (Basel). 12 (2022). https://doi.org/10.3390/met12030503.

[30] M.J. Ranjbar Naserabadi, S. Sodagar, Application of Phased Array Ultrasonic Transducers for Guided Wave Scanning of Plates Using Multi-point Focusing Technique, J. Nondestruct. Eval. 41 (2022). https://doi.org/10.1007/s10921-022-00867-0.

[31] W.A.K. Deutsch, A. Cheng, J.D. Achenbach, Self-focusing of rayleigh waves and lamb waves with a linear phased array, Res. Nondestruct. Eval. 9 (1997) 81–95. https://doi.org/10.1080/09349849709409609.

[32] K.C.T. Nguyen, L.H. Le, T.N.H.T. Tran, M.D. Sacchi, E.H.M. Lou, Excitation of ultrasonic Lamb waves using a phased array system with two array probes: Phantom and in vitro bone studies, Ultrasonics. 54 (2014) 1178–1185. https://doi.org/10.1016/j.ultras.2013.08.004.

[33] R.B. Randall, Frequency analysis., Bruel and Kjaer, Naerum, Denmark, 1987.

[34] B.A. Auld, G.S. Kino, Normal Mode Theory for Acoustic Waves and its Application to the Interdigital Transducer, IEEE Trans. Electron Devices. 18 (1971) 898–908. https://doi.org/10.1109/T-ED.1971.17303.

[35] J.D. Achenbach, Reciprocity in elastodynamics, Cambridge University Press, 2003.

[36] Y.F. Xing, B. Liu, Exact solutions for the free in-plane vibrations of rectangular plates, Int. J. Mech. Sci. 51 (2009) 246–255. https://doi.org/10.1016/j.ijmecsci.2008.12.009.

[37] R.R. Craig, Structural Dynamics: An Introduction to Computer Methods, Wiley, 1981.

[38] E. Paraskevopoulos, S. Natsiavas, On application of Newton's law to mechanical systems with motion constraints, Nonlinear Dyn. 72 (2013) 455–475. https://doi.org/10.1007/s11071-012-0727-1.

[39] S.-C. Wooh, Y. Shi, Optimum beam steering of linear phased arrays, 1999.

[40] E. V. Glushkov, N. V. Glushkova, O. V. Kvasha, R. Lammering, Selective Lamb mode excitation by piezoelectric coaxial ring actuators, Smart Mater. Struct. 19 (2010). https://doi.org/10.1088/0964-1726/19/3/035018.

[41] D. Lines, J. Wharrie, J. Hottenroth, Multi-Channel Ultrasound Toolbox: A Flexible Modular Approach for Real-Time Array Imaging and Automated Inspection, 2010.

[42] D. Alleyne, P. Cawley, A two-dimensional Fourier transform method for the measurement of propagating multimode signals, J. Acoust. Soc. Am. 89 (1991) 1159–1168. https://doi.org/10.1121/1.400530.

[43] P.D. Wilcox, Omni-directional guided wave transducer arrays for the rapid inspection of large areas of plate structures, IEEE Trans. Ultrason. Ferroelectr. Freq. Control. 50 (2003) 699–709. https://doi.org/10.1109/TUFFC.2003.1209557.

[44] R. Sicard, J. Goyette, D. Zellouf, A SAFT algorithm for lamb wave imaging of isotropic plate-like structures, Ultrasonics. 39 (2002) 487–494. https://doi.org/10.1016/S0041-624X(01)00087-7.

[45] B. Ghose, R.S. Panda, K. Balasubramaniam, Phase velocity measurement of dispersive wave modes by Gaussian peak-tracing in the f-k transform domain, Meas. Sci. Technol. 32 (2021). https://doi.org/10.1088/1361-6501/ac261b.

[46] A. Huber, Dispersion Calculator (DC), (2018). https://www.dlr.de/zlp/en/desktopdefault.aspx/tabid-14332/0A24874_read-61142/#/gallery/33485.